ACS Catalysis

pubs.acs.org/acscatalysis Research Article

Potential Dependence of the Local pH in a CO_2 Reduction Electrolyzer

Danielle A. Henckel, Michael J. Counihan, Hannah E. Holmes, Xinyi Chen, Uzoma O. Nwabara, Sumit Verma, Joaquín Rodríguez-López, Paul J. A. Kenis,* and Andrew A. Gewirth*

Cite This: *ACS Catal.* 2021, 11, 255−263 Read Online

ACCESS | Metrics & More | Article Recommendations | Supporting Information

ABSTRACT: Quantifying the local pH of a gas diffusion electrode undergoing CO_2 reduction is a complicated problem owing to a multitude of competing processes, both electrochemical- and transport-related, possibly affecting the pH at the surface. Here, we present surface-enhanced Raman spectroscopy (SERS) and electrochemical data evaluating the local pH of Cu in an alkaline flow electrolyzer for CO_2 reduction. The local pH is evaluated by using the ratio of the SERS signals for HCO_3^- and CO_3^{2-}. We find that the local pH is both substantially lower than expected from the bulk electrolyte pH and exhibits dependence on applied potential. Analysis of SERS data reveals that the decrease in pH is associated with the formation of malachite [$Cu_2(OH)_2CO_3$, malachite] due to the presence of soluble Cu(II) species from the initially oxidized electrode surface. After this initial layer of malachite is depleted, the local pH maintains a value >11 even at currents exceeding −20 mA/cm^2.

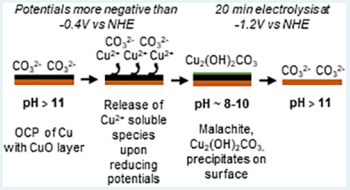

KEYWORDS: *CO_2 reduction, local pH, flow electrolyzer, gas diffusion electrode, surface-enhanced Raman spectroscopy*

1. INTRODUCTION

The rising level of CO_2 in the atmosphere, and associated climate change effects, has led to numerous research investigations on CO_2 mitigation as well as utilization. Among these strategies is the electroreduction of CO_2 into value-added C_1 (CO and formate) and C_2 (ethylene, ethanol, and acetate) products.[1−3] Research on CO_2 reduction has focused on catalyst and electrode development for product selectivity and is moving toward achieving durability and scaling.[4,5] Oftentimes, studies evaluating catalysts for the CO_2 reduction reaction (CO_2RR) utilize a traditional electrochemical H-cell in small-scale laboratory experiments. Poor solubility of CO_2 in water (~34 mM) limits the achievable current densities, typically less negative than −10 mA/cm^2, which prevents the application of H-cells at a scale in an economically feasible fashion.[4] To circumvent this issue, gas diffusion electrodes (GDEs) are utilized because they enable delivery of CO_2 at a high concentration to the surface of the catalyst at the triple phase boundary by separating the electrolyte and the gas streams.[5] In addition to the GDE, utilizing a flow cell minimizes pH gradients at the surface of the cathode and anode. The flowing electrolyte reduces the width of the depletion boundary layer, thus replenishing the electrolyte and potentially outcompeting CO_2 buffer reactions (eq 1−3). Best performance in terms of current densities and low overpotentials is typically achieved using alkaline electrolytes based on hydroxide salts.[6,7] However, the hydroxide can react with CO_2 (eqs 1 and 2) to form carbonate species, which in turn influences the local pH of the electrode surface.

Cu is an important catalyst for CO_2 reduction, as it is the only single metal catalyst that can reduce CO_2 into C_{2+} products at relevant rates.[4] Others have already demonstrated that the local pH of a GDE under CO_2RR conditions is an important parameter in determining the product selectivity on Cu.[8−13] While the pH of the bulk electrolyte can be measured at the inlet and outlet, the exact pH at the electrode surface is expected to vary from the bulk because of the involvement of the OH^- species in the reactions occurring at both electrodes. Only few studies have sought to characterize the pH at the surface of GDEs under operating conditions experimentally, although calculations have been reported.[6,14,15]

The local pH of a Cu electrode has been proposed to be associated with Cu speciation.[16] The Pourbaix diagram of the Cu−H_2O−CO_2 ternary system depicts many different Cu phases such as copper oxide (Cu_2O, CuO) and copper carbonate (azurite, malachite) species.[17] According to this diagram, only Cu(0) is stable at potentials greater (more negative) than −0.4 V,[17] although the kinetics of the reduction of oxidized Cu phases are slow on the time scale of CO_2 reduction.[16]

As the CO_2RR under neutral or basic conditions generates OH^- equivalents (eq 4), an increase in the current will lead to an increase in the local pH in an H-cell[18−20] as well as a zero-gap HCO_3^- flow cell.[21] Published computational models agree with this assumption and have found that the local pH of a

Received: October 2, 2020
Revised: November 30, 2020
Published: December 18, 2020

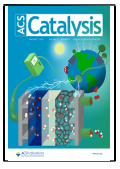

https://dx.doi.org/10.1021/acscatal.0c04297
ACS Catal. 2021, 11, 255−263

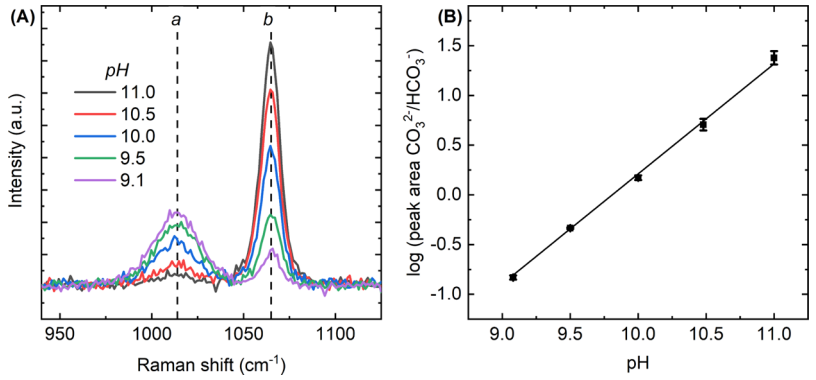

Figure 1. (A) SERS spectra of electrodeposited Cu on a GDE in solutions of different pHs containing $KHCO_3$ (peak *a*) and K_2CO_3 (peak *b*) totaling 1 M electrolyte concentration. (B) Calibration curve for local pH utilizing the HCO_3^- (peak *a*) and CO_3^{2-} (peak *b*) peak area ratio.

GDE in an alkaline flow cell is ∼10 at −0.8 V, and upon increasing the potential to −1.4 V, the pH rises above 14.4.[14]

$$CO_2 + OH^- \leftrightarrow HCO_3^- \quad (1)$$

$$CO_2 + H_2O \leftrightarrow HCO_3^- + H^+ \quad (2)$$

$$HCO_3^- + OH^- \leftrightarrow CO_3^{2-} + H_2O \quad (3)$$

$$aCO_2 + b(H_2O + e^-) \leftrightarrow \text{products} + m\text{OH} \quad (4)$$

More recent work demonstrated the presence of a pH gradient extending ∼100 μm from the surface of a GDE in the bulk electrolyte in alkaline flowing conditions using Raman spectroscopy. The 100 μm electrolyte layer adjacent to the GDE was shown to contain HCO_3^-, owing to the reaction of the electrolyte with CO_2 (eq 3), thus demonstrating a pH gradient.[15] In this work, the closest distance to the electrode surface that the pH is measured is 10 μm. This pH gradient will be affected by the width of the boundary layer resulting from cell design and experimental parameters.

Both SERS and SEIRAS (surface-enhanced infrared absorption spectroscopy) are commonly used as in situ techniques to probe Cu surfaces, as they both provide a surface-enhanced signal. Utilizing SERS as a measure of local pH is preferable to SEIRAS because of the spectral convolution of overlapping peaks of HCO_3^- and CO_3^{2-} in SEIRAS. In contrast, the HCO_3^- and CO_3^{2-} peaks in Raman spectra that can be used to measure the local pH, appear as individual, well-separated peaks in the 950−1100 cm^{-1} spectral region. Typically, SERS interrogates ∼3 nm from the surface of the plasmonic metal.[22] This distance would equate to a layer of ∼14 CO_3^{2-} molecules if oriented in an end-on fashion. In contrast to a previous report on the pH in a GDE in an alkaline flow cell, we observe the local pH within this 3 nm layer.[15]

In this work, we report local pH data of a Cu GDE in an alkaline flow cell under CO_2 reduction conditions via surface-enhanced Raman spectroscopy (SERS) utilizing the HCO_3^- and CO_3^{2-} peak area ratios. Observing the local pH in a flow cell configuration allows studying the impact of current densities more negative than −20 mA/cm^2 and a high local concentration of CO_2. Importantly, the setup of the spectroscopic flow cell configuration has similar dimensions as and is operated similar to the flow cell configurations used for detailed catalyst and electrode performance characterization.

2. EXPERIMENTAL SECTION

2.1. Preparation of Electrodes. The electrodeposited Cu electrodes were prepared via electrodeposition onto Sigracet 35BC GDEs using 3,5-diamino-1,2,4-triazole as an electrodeposition inhibitor to the electroplating bath.[23] The anode electrodes were prepared by spray-coating IrO_2 (Alfa Aesar) and a Nafion binder onto a Sigracet 35BC GDE as previously reported.[24] The anode loading was 2 ± 0.2 mg/cm^2 IrO_2, and the cathode loading was ∼0.7 mg/cm^2 Cu. The geometric surface area for the Cu electrode was 1 cm^2. The anode was typically a 2 mm × 5 mm rectangle placed on a stainless steel current collector. Cu electrodes were deposited between 24 and 36 h before SERS measurements, resulting in oxidation from ambient conditions. The typical electrochemical active surface area for this Cu electrode preparation was determined to be ∼7 cm^2 by using the Pb_{upd} stripping wave.[23]

2.2. SERS and Characterization of Electrodes. In situ SERS measurements were performed with a custom spectroscopic Raman flow cell[25] described previously.[26,27] A 531.9 nm laser (B&W Tek) provided sample excitation at approximately 45° relative to an 85 mm f/1.2 collection lens (Canon). The scattered radiation was then focused using an f/3.3 lens to the 50 μm slit of a SpectraPro 2300i monochromator (Princeton Instruments) with grating of 1200 grooves per mm. The charge coupled device detector (Andor) was thermoelectrically cooled to −80 °C. Typical spectral resolution was estimated to be 6 cm^{-1}. Acquisition time was 1 s, and the total accumulation of scans was 60 for the calibration curve and 120 for subsequent data. Error bars were obtained from at least three independent measurements. CO_2 and Ar flow rates were maintained with a mass flow controller (Smart-Trak 2, Sierra Instruments). In experiments with mixed gases, a t-valve was used to mix the gases. A Ag/AgCl reference (BASi, RE-5B) in the cell enabled direct measurement of the cathode potential. All potentials are reported with respect to NHE. Scanning electron microscopy (SEM) images were obtained utilizing a JEOL 7000F Analytical SEM. X-ray diffraction (XRD) patterns were obtained using a Bruker D8 ADVANCE X-ray Diffractometer.

2.3. pH Calibration. The calibration curve for local pH was created by measuring the SERS spectra of a Cu surface in different concentrations of $KHCO_3$ and K_2CO_3, totaling 1 M concentration of electrolyte flowing into the Raman cell at 0.5 mL/min. The peaks were fit to a Lorentzian shape. The bulk pH was measured using a pH meter. All chemicals were purchased from Sigma Aldrich or Fisher Scientific and used as received—KOH (99.99% semi-conductor grade), $KHCO_3$

https://dx.doi.org/10.1021/acscatal.0c04297
ACS Catal. 2021, 11, 255−263

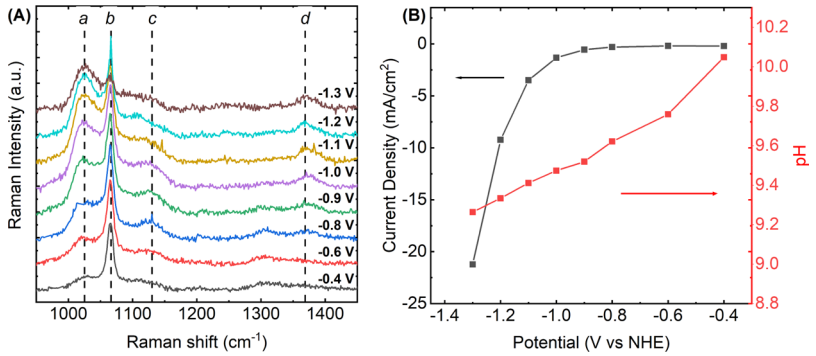

Figure 2. (A) SERS spectra of an electrodeposited Cu GDE with 1 M KOH flowing over the electrode and 12 sccm CO_2 on the backside of the electrode as the potential is increased from −0.4 to −1.3 V versus NHE and (B) current density and local pH as a function of potential, averaged from three runs.

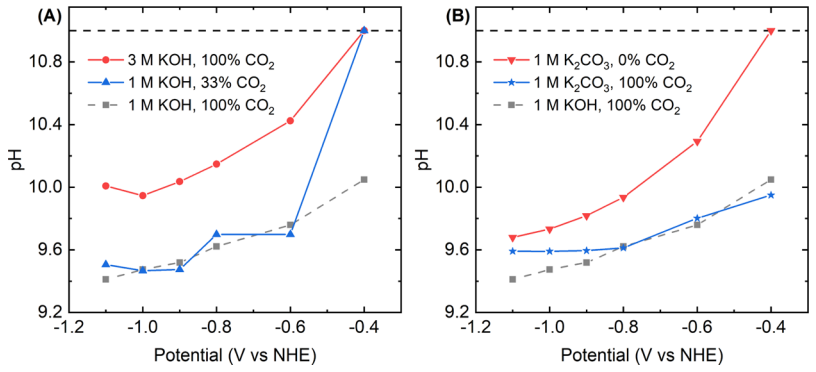

Figure 3. (A) Local pH of an electrodeposited Cu GDE with 3 M KOH, 100% CO_2 (red trace), 1 M KOH, 33% CO_2 (blue trace), and 1 M KOH, 100% CO_2 (gray, data from Figure 2B) as the potential is increased reductively and (B) local pH of the Cu GDE with 1 M K_2CO_3, 0% CO_2 (red), 1 M K_2CO_3, 100% CO_2 (blue), and 1 M KOH, 100% CO_2 (gray, data from Figure 2B). The LOD is pH of 11.0 and shown as a dotted, black line.

(98%), and K_2CO_3 (98%). All solutions were prepared using Millipore Mill-Q water (18 MΩ).

3. RESULTS

3.1. Local pH on Cu Electrodes. To investigate the change of the pH at or near the surface of the electrode, we measured the Raman peak intensities for HCO_3^- and CO_3^{2-} on a Cu GDE (under no applied potential) placed inside our spectroscopic flow cell as a function of bulk pH. Figure 1A shows the SERS data obtained from Cu electrodeposited onto a GDE surface in solutions containing different bulk pHs of $KHCO_3$ and K_2CO_3 totaling 1 M concentration. Two peaks at 1014 cm^{-1} (peak *a*) and 1065 cm^{-1} (peak *b*) are present in this spectral region. Peak *a* is associated with the C−OH stretch (A′) of HCO_3^-, while peak *b* is associated with the total symmetric C−O stretch of carbonate (A_1').[28] Additionally, peak *a* is substantially broader (∼6) and less intense than peak *b*, a feature reported previously.[29] The greater peak width for peak *b* may be due to a wider distribution of vibrational energies due to solution interactions.[28] We note that peak *a* was not observed in prior SERS measurements obtained using a 0.1 M HCO_3^- electrolyte under similar conditions.[30−32] This absence may be due to the use of lower concentrations (0.1 M) of HCO_3^- and the inherent broadness of the peak, resulting in the loss of this peak to the baseline.

The CO_3^{2-}/HCO_3^- peak intensity ratio relates to the relative amounts of CO_3^{2-} and HCO_3^- at or near the Cu electrode surface.[22] To quantify the relationship between the CO_3^{2-}/HCO_3^- peak intensity ratio and the local pH, we performed calibration measurements using SERS by taking spectra at different bulk pH values. This CO_3^{2-}/HCO_3^- ratio has been associated with pH dependence previously.[28] Figure 1B shows the calibration curve obtained by measuring the relative peak area ratios as a function of pH by using the SERS data obtained from electrodeposited Cu in Figure 1A. Figure 1B shows that the log of the peak area ratios of CO_3^{2-}/HCO_3^- is linear as a function of bulk pH solution. This relationship is expected from the Henderson−Hasselbach equation for a CO_3^-/HCO_3^- system (eq 5).

$$\mathrm{pH} = \mathrm{p}K_a + \log\left(\frac{\mathrm{CO_3}^{2-}}{\mathrm{HCO_3}^-}\right) \quad (5)$$

3.2. Local pH in a Flow Cell. Next, we performed in situ SERS on an electrodeposited Cu GDE under potential control. Figure 2A shows the SERS spectra obtained with gas and electrolyte flow rates of 12 sccm (standard cubic centimeters per minute) CO_2 and 0.5 mL/min 1 M KOH, respectively. The cathode potential was swept from −0.4 to −1.3 V vs NHE in 0.1 V increments, remaining at each potential for 126 s (the spectra are an average of 120 acquisitions). These potentials extend into CO_2-reducing potentials for this catalyst.[23] As seen in Figure 2B, at more negative potentials, the CO_3^{2-}/HCO_3^- ratio decreases, corresponding to a decrease in the local pH. The peaks corresponding to HCO_3^- and CO_3^{2-} are not shifted within error from their solution values. Additionally, peak *c* and *d* appear at ∼1130 and 1370 cm^{-1}, respectively. These peaks are associated with the carbonate-centered modes of $Cu_2CO_3(OH)_2$ (basic copper carbonate or malachite).[33]

https://dx.doi.org/10.1021/acscatal.0c04297
ACS Catal. 2021, 11, 255−263

In order to understand how CO_2 electrolysis conditions affect the local pH, we examined the local pH for the Cu GDE with either increased KOH concentration (3 M KOH) or decreased CO_2 concentration (33%) in the feed (8 sccm Ar, 4 sccm CO_2). Figure 3A shows that increasing [OH^-] from 1 to 3 M at 100% CO_2 feed (gray and red traces, respectively) results in an initial pH > 11.0 outside the limit of detection (LOD) at −0.4 V, which is an increase of 1 pH unit relative to the 1 M case. With a decrease in potential to −1.1 V, the pH in the 3 M case drops to 10.0, again substantially higher than the pH of 9.4 seen in the 1 M case. Figure 3A also shows the effect of decreased [CO_2] in the gas feed at 1 M KOH. With only 33% CO_2 in the feed, the initial pH is again >11.0, one pH unit higher than that seen with 100% CO_2 at −0.4 V. However, the pH decreases with decreasing potential to a value of 9.5 at −1.1 V.

Figure 3B shows the local pH obtained in a solution of 1 M K_2CO_3 with and without the presence of CO_2 in the gas flow (blue and red traces, respectively). The figure shows that in the absence of CO_2 in the gas flow but in the presence of K_2CO_3, the pH at −0.4 V is higher than that obtained with CO_2 in the gas flow. The local pH also decreases with potential in both experiments. When the gas flow consists of 100% CO_2, the pH decreases to values similar to that seen in the 1 M KOH case. The data show that the presence of flowing CO_2 leads to a diminished pH relative to the solution containing only K_2CO_3. This decrease suggests that the dissolved CO_2 helps to reduce the pH. Additionally, there is a potential-dependent decrease in the pH without the presence of CO_2 in the gas flow, but with an electrolyte containing K_2CO_3.

To understand the correlation between the appearance of peak *c*, corresponding to malachite, and peaks *a* and *b* corresponding to HCO_3^- and CO_3^{2-}, respectively, the integrated peak areas for these peaks versus potential are shown in Figure S1A, where 1 M K_2CO_3 was the electrolyte. In the experiment without CO_2, the peak areas for HCO_3^- and malachite increase together as the potential is made more negative. In contrast, peak areas for CO_3^{2-} remain relatively constant. In Figure S1B, the peak areas with 1 M K_2CO_3 as the electrolyte and 100% CO_2 in the gas flow are shown. Here, peak areas for HCO_3^- and malachite exhibit similar potential dependence. At ∼ 0.9 V, the potential for the onset of CO_2 reduction, both the HCO_3^- and malachite peak areas decrease. This decrease in the peak area may be due to displacement by other species, such as CO, that form during CO_2 reduction on the Cu surface.

3.3. Origin of Increased Surface Acidity. One of the most interesting features of the pH vs potential plots shown in Figures 2 and 3 is the roughly linear dependence of pH on potential. Interestingly, the pH changes even at potentials where little or no CO_2 reduction activity occurs. This fact suggests that the change in pH at or near the Cu electrode surface is associated with potential-dependent changes in the Cu itself in combination with the presence of CO_3^{2-}. We note that the presence of malachite, as seen in SERS, requires Cu(II) availability.

At the open circuit potential (OCP) (∼0.0 V vs NHE) in alkaline conditions, prior work suggests that the Cu surface exists as a layered structure consisting of Cu (bottom), Cu_2O (middle), and CuO (top).[34,35] The Raman spectra of Cu at the OCP under flowing 1 M KOH and 12 sccm CO_2 exhibit bands at 420, 529, and 620 cm^{-1} (Figure S2), which can be assigned to Cu_2O.[32,36−38] We note that the CuO (633 cm^{-1}) and Cu_2O (620 cm^{-1}) Raman band can overlap; thus, we do not rule out the presence of CuO at the OCP.[36,39] The Cu surface at the OCP is likely composed of a mixed oxide with both Cu(I) and Cu(II) contributions.[17] A layer of $Cu(OH)_2$ may also be present on the surface in alkaline conditions depending on the surface history with regard to oxidation,[38] although this band (∼460 cm^{-1}) can be weak and possibly convoluted within the oxide region.[36] We note that the initial linear sweep voltammogram from the Cu surface (Figure S3) exhibits peaks corresponding to the reduction of $Cu(OH)_2$ to Cu_2O at −0.70 V and reduction of Cu_2O to Cu(0) at −0.78 V.[34]

The Pourbaix diagram for the Cu−H_2O−CO_2 ternary system[17] shows that Cu is not stable in strongly alkaline (pH = 14) environments at potentials more positive than ∼ −0.4 V. Instead, the Cu surface dissolves to form soluble Cu(II) species at pH values above ∼9.[40] As the pH is lowered, a region of stability at more positive potentials occurs because of the formation of CuO.[17]

Experimentally, in the potential region between −0.2 and −1.0 V versus NHE, prior work shows that the oxidized Cu surface in alkaline conditions exhibits a number of potential-dependent changes.[34,35,41−44] In particular, force curves obtained in this region show the presence of long range forces (ca. 100−200 nm) associated with the presence of soluble species dissolving from the Cu surface.[43] Interestingly, these soluble species are present at potentials more positive (starting at 0.1 V) than the first Cu(II) to Cu(I) reduction wave, which occurs at ca. −0.3 V and persist until at least −0.6 V. The maximum of soluble species production occurs in the potential region around −0.3 V. The Cu(II) to Cu(I) reduction wave was found to exhibit a 0.84 power dependence on the scan rate, suggesting that this wave is associated with the reduction of both soluble and surface-confined species. Rotating ring disk electrode measurements also show the presence of dissolved Cu(II) originating either from Cu(II) dissolution or disproportionation of Cu(I) species in the potential region from 0 to −0.3 V in 0.1 M NaOH.[44] In addition, the reduction of CuO to Cu_2O also promotes the release of Cu(II) ions that can reach supersaturation and precipitate as a $Cu(OH)_2$ layer on top of Cu_2O under alkaline conditions at ∼0.160 V versus NHE.[45−47]

The presence of soluble species at potentials positive of the Cu(II) reduction wave suggests that some of the soluble species are in fact Cu(II) complexes. Candidate complexes include copper hydroxide species [$Cu(OH)_n^{2-n}$] and copper carbonate species [$CuCO_3$ or $Cu(CO_3)_2^{2-}$].[17] The exact speciation of Cu(II) in this environment depends on [Cu(II)], [CO_3^{2-}], and pH.[40,48−50] Thus, the production of soluble Cu(II) species is potential-dependent and increases as the potential becomes more negative.

The presence of soluble Cu(II) species provides a mechanism by which malachite formation may occur, as seen in SERS.[22] Copper carbonate minerals (malachite and/or azurite) have been observed on the surface of CuO materials reduced under Ar-saturated $KHCO_3$ previously, although not observed under CO_2-saturated $KHCO_3$.[31] Malachite has the lowest solubility constant of possible precipitating species ($K_{sp,Cu_2(OH)_2CO_3} = 10^{-33.31}$, $K_{sp,Cu(OH)_2} = 10^{-19.33}$, $K_{sp,CuCO_3} = 10^{-11.5}$) in this alkaline, carbonate-containing electrolyte.[48] Malachite was the major component of precipitates observed upon addition of Na_2CO_3 to a solution of Cu(II) in solutions of pH 8.[48] Among pathways to form $Cu_2CO_3(OH)_2$, either

https://dx.doi.org/10.1021/acscatal.0c04297
ACS Catal. 2021, 11, 255−263

copper hydroxides ($Cu(OH)_n^{2-n}$) or Cu(II) (eqs 6–8) yield high equilibrium constants.[49−51] Of these candidate reactions, eqs 6 and 7 would cause the lowering of the pH by the consumption of carbonate and are likely the dominant reaction(s) taking place. The precipitation of malachite consumes carbonate and lowers the effective pH at the surface.

$$2Cu^{2+} + 2OH^- + CO_3^{2-} \leftrightarrow Cu_2CO_3(OH)_2(s) \quad K = 10^{32} \tag{6}$$

$$2CuOH^+ + CO_3^{2-} \leftrightarrow Cu_2CO_3(OH)_2(s) \quad K = 10^{20} \tag{7}$$

$$2Cu(OH)_2 + CO_3^{2-} \leftrightarrow Cu_2CO_3(OH)_2(s) + 2OH^- \quad K = 10^{57} \tag{8}$$

$$2Cu(OH)_4^{2-} + CO_3^{2-} \leftrightarrow Cu_2CO_3(OH)_2(s) + 6OH^- \quad K = 10^{83} \tag{9}$$

After removing the potential, the surface returns to OCP, which is ca. 0 V. In SERS, only the CO_3^{2-} band is observed, which suggests the pH to be >11. This observation suggests that CO_3^{2-} consumption is no longer occurring. One possibility for this increase in pH is the cessation of Cu(II) production, and thus malachite formation, once the potential is made more positive. Another possibility is that the $Cu_2CO_3(OH)_2$ layer converts to CuO as the potential is brought back to OCP. The peak reduction potential for malachite was observed at −0.34 V versus NHE (0.1 M $Na_2B_4O_7$).[52] The malachite layer must be kinetically persistent, as it is observed here at potentials much more reducing.

Figure S4A shows the time dependence of the SERS spectrum obtained with flowing 1 M KOH and 12 sccm CO_2 at −1.4 V following a sequence where the potential is changed from −0.4 to −1.4 V. The figure shows that the CO_3^{2-}/HCO_3^- ratio changes during this time. Figure S4B shows the time dependence of the local pH value. The figure shows that the pH changes from ∼9.6 to ∼10.2 over a period of 20 min (Figure S4). We suggest that the origin of this pH change is depletion of soluble Cu(II) after reduction of the oxide layer is complete. SEM images obtained before and after the potential hold reveal the increased presence of textured features after the potential hold (Figure S5). These features may be a consequence of Cu redeposition. XRD patterns after electrolysis show only the presence of CuO, Cu_2O, and $Cu(OH)_2$ (Figure S6). These are expected products from a Cu electrode exposed to an alkaline solution following the removal of the applied potential prior to cell disassembly.

3.4. Kinetics of CO_3^{2-} and HCO_3^- Formation and Depletion. The local pH measurements in Figures 2 and 3 show that the Cu surface is more acidic than the bulk pH of 14 expected for 1 M KOH. Next, we investigated the origin of the increase in the HCO_3^-/CO_3^{2-} ratio utilizing eqs 1–4 and 6. HCO_3^- is continually formed in an alkaline flow electrolyzer by the reaction of CO_2 and OH^- (eq 2). The rate constant of this reaction in solution is 2.23×10^3 L mol^{-1} s^{-1}.[53] CO_3^{2-} is formed only through the deprotonation of HCO_3^- (eq 3). The rate constant for HCO_3^- deprotonation is 6.0×10^9 L mol^{-1} s^{-1}. Owing to the large deprotonation rate of HCO_3^-, more than 6 orders of magnitude larger than its formation rate constant, the local pH of the Cu GDE is expected to be alkaline.

To accurately model the surface concentrations of HCO_3^- and CO_3^{2-}, we also measured the desorption (k_d) and adsorption (k_a) rates of CO_3^{2-} and HCO_3^- following a previously reported method utilizing a spectroscopic flow cell.[54] The values for k_a were measured by flowing 1 M $KHCO_3$ or K_2CO_3 over the Cu GDE and monitoring the Raman peak areas over time. The k_d values were measured by flowing H_2O over Cu, on which $KHCO_3$ or K_2CO_3 was previously adsorbed (Figure S6). Here, we found the following values: $k_d^{HCO_3^-} = 0.003$ s^{-1}, $k_a^{HCO_3^-} = 0.03$ s^{-1}, $k_d^{CO_3^{2-}} = 0.003$ s^{-1}, and $k_a^{CO_3^{2-}} = 0.03$ s^{-1}. The adsorption rates for both HCO_3^- and CO_3^{2-} were 10-fold larger than their corresponding desorption rates, showing the affinity of carbonate species toward the Cu surface.

To determine how electrode potential and the presence of malachite impact the local pH equilibrium in a flow cell with 1 M KOH and 100% CO_2 gas flow (same conditions as Figure 1), we used a model to determine the relative rate constants of protonation (k_{prot}) and deprotonation (k_{deprot}) of CO_3^{2-} and HCO_3^- on or near the catalyst surface. This simple model treats these rates as pseudo-first order processes, as water (proton source) and hydroxide (deprotonating species) availability should not be rate-limiting here. Given the known adsorption and desorption rates of CO_3^{2-} and HCO_3^-, and treating the malachite and oxide as site-blocking surface species, the surface concentrations of CO_3^{2-} and HCO_3^- are controlled by k_{prot} and k_{deprot}, which can also be described as an apparent equilibrium constant K_{surf}

$$CO_3^{2-}{}_{surf} \underset{k_{deprot}}{\overset{k_{prot}}{\longleftrightarrow}} HCO_3^-{}_{surf} \tag{10}$$

$$K_{surf} = \frac{k_{prot}}{k_{deprot}} \tag{11}$$

Our model uses the Raman data in a semiquantitative treatment. Because SERS enhancement factors are strongly dependent on field strength and distance, absolute quantification of surface coverage is not possible here. However, we compared the relative peak areas of all species (CO_3^{2-}, HCO_3^-, $CuCO_3(OH)_2$, and $Cu_{(2)}O$) across all potentials and assigned percentages of total surface coverage, as described in the Supporting Information. Here, we assume that the Raman cross sections are the same across all species. This treatment provides a zeroth-order approximation to relative surface coverages. This kinetic model describes the evolution of CO_3^{2-} and HCO_3^- coverage over time, again given that the malachite and the copper oxide coverage are constant at a given condition,

$$\frac{d\Gamma_{HCO_3^-}}{dt} = (k_a^{HCO_3^-} \times \Gamma_*) - (k_d^{HCO_3^-} \times \Gamma_{HCO_3^-}) + (k_{prot} \times \Gamma_{CO_3^{2-}}) - (k_{deprot} \times \Gamma_{HCO_3^-}) \tag{12}$$

$$\frac{d\Gamma_{CO_3^{2-}}}{dt} = (k_a^{CO_3^{2-}} \times \Gamma_*) - (k_d^{CO_3^{2-}} \times \Gamma_{CO_3^{2-}}) - (k_{prot} \times \Gamma_{CO_3^{2-}}) + (k_{deprot} \times \Gamma_{HCO_3^-}) \tag{13}$$

$$\Gamma_* = \Gamma_{max} - \Gamma_{HCO_3^-} - \Gamma_{CO_3^{2-}} - \Gamma_{malachite} - \Gamma_{oxide} \tag{14}$$

where Γ_* represents the coverage of available sites for CO_3^{2-} and HCO_3^- binding and Γ_{max} is an arbitrary maximum number

https://dx.doi.org/10.1021/acscatal.0c04297
ACS Catal. 2021, 11, 255−263

of surface sites to which the coverage of all species can be normalized. Assuming each measurement is at equilibrium and thus utilizing steady-state approximations, K_{surf} (eq 11) was calculated based on the relative CO_3^{2-} and HCO_3^- Raman signals and pH (eq 5).

Within the pH regime experimentally accessible and using the observed HCO_3^-/CO_3^{2-} ratio, plausible k_{prot} and k_{deprot} values were determined for each electrode potential. Details on fitting can be found in the Supporting Information. The K_{surf} was then calculated and plotted as a function of potential, along with HCO_3^- and malachite coverages (Figure 4).

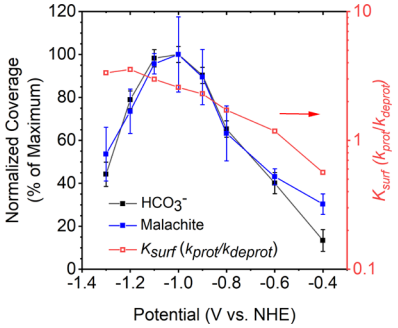

Figure 4. Correlation of calculated surface protonation equilibrium constant (K_{surf}) with estimated normalized HCO_3^- and malachite coverage as a function of electrode potential. The calculation of normalized coverages via relative Raman intensities is described in the text and Supporting Information.

Decreasing the electrode potential increases the malachite coverage to a maximum coverage ~ −1.0 V, and this coincides with an increase in the protonation rate constant and decrease in the deprotonation rate constant (higher K_{surf}). Because the reduction of the surface oxide drives the formation of malachite and the pH change, we expect the potential dependence to arise from potential dependence of the rate of surface oxide reduction. Importantly, this decrease in the effective deprotonation rate constant reflects the consumption of CO_3^{2-} and/or OH^- ions during malachite formation. Malachite and HCO_3^- reach their maximum coverage at −1.0 V. This potential aligns with the onset of CO_2 reduction, which represents another pathway through which HCO_3^- can be consumed. The coverage of CO_3^{2-} also decreases past this potential (Figure S8), keeping the pH in the range of 9.2−9.4 past −1.0 V (Figure 2B). This additional consumption path of HCO_3^- would impact the observed effective rate constants as well as the changes in the rate of malachite formation.

4. DISCUSSION

The results above show that the pH in the flow cell environment is not constant but rather changes to lower values as a function of applied potential. This change in pH occurs before the passage of substantial current associated with CO_2 reduction. The results show that a sink for CO_3^{2-} and OH^- is the formation of malachite by reaction with soluble Cu(II) species. Modeling shows that the $k_{prot}/k_{deprot} = K_{surf}$ also must change as a function of applied potential on the Cu electrode surface.

4.1. pH Change. As the potential is made more negative from −0.4 V in the presence of flowing CO_2, the pH at the Cu electrode surface changes from 10.4 to 9.3 at −1.2 V. In addition to the increased relative concentration of HCO_3^-, used to evaluate the pH, characteristic bands for malachite are observed. The Raman band areas for HCO_3^- and malachite increase simultaneously (Figure S1). In the potential range evaluated here, soluble Cu(II) is continuously formed, likely during CuO reduction.[43−47] This Cu(II) will precipitate as $Cu_2(OH)_2CO_3$ because of the carbonate-rich environment at the Cu surface.

Interestingly, $Cu_2CO_3(OH)_2$ is most thermodynamically stable in the pH range of 8.0−10.5.[55] The Pourbaix diagram suggests that $Cu_2CO_3(OH)_2$ should not exist at potentials more negative than 0.0 V versus NHE, although this species may persist if its reduction is kinetically slow or the reduction produces free Cu(II) ions which in turn restart the malachite formation process. Thus, the origin of the increased K_{surf} seen in Figure 4 is the persistent formation of malachite due to Cu(II) dissolution during the reductive sweep.

Another origin of the increased HCO_3^- could be at the surface of the malachite itself. At the potential of zero charge (E_{pzc}), the pH at the surface of malachite, or the pH_{pzc}, is 8.0. This pH value is due to the two potential-determining ions on the malachite surface, HCO_3^- and $CuOH^+$.[56] HCO_3^- is positioned at the octahedral apex of Cu(II) on the surface, and the bond is described as a weak van der Waals type.[56] The exact ratio of these two potential-determining ions depends on the potential distance from E_{pzc}. E_{pzc} of a bare Cu surface in alkaline is thought to be at ca. −0.7 V, indicating that anion association with the surface should dominate at the potentials considered here.[57]

4.2. Depletion of Malachite. The depletion of the malachite layer varies from ~20 to 40 min depending on applied potential and electrode. As this layer is depleted, the local pH at the Cu surface increases because there is no longer a sink for CO_3^{2-}. Figure S8 shows the potential-dependent SERS obtained from a Cu electrode following malachite depletion and oxide reduction in 1 M KOH, with 12 sccm flowing CO_2 from −0.4 to −1.2 V versus NHE. Figure S8 also shows that only a carbonate signal is observed, suggesting that the local pH is >11.0. Thus, the pH drop observed prior to surface reduction reflects the presence of cupric oxides and the availability of the malachite sink for CO_3^{2-}. A recent report detailed pH measurements in the 130 μm layer of the electrolyte adjacent to the electrode surface measured using Raman in an alkaline flow cell. An acidic pH was observed at 10 μm and persisted until ~100 μm into the solution.[15] In contrast, in our work when utilizing SERS, the signal is typically enhanced only up to 3 nm from the electrode surface, and in this sample volume, we do not observe an acidic pH-absent malachite formation.[22] Because our surface is more alkaline than the previous report, the exact dimensions of the cell and thus the Nernst layer is likely to account for the difference.

Our data and model describe the shift in HCO_3^-/CO_3^{2-}equilibrium at the Cu surface as the potential decreases and malachite forms at the Cu surface. The malachite acts as a carbonate sink as Cu(II) dissolves and then precipitates as $Cu_2CO_3(OH)_2$. This process creates a local pH decrease at the Cu surface which is detectable via the HCO_3^- and CO_3^{2-} SERS signals. At much lower potentials (past −1.2 V) or at much longer timescales (20 + minutes of reduction), the malachite is fully reduced (thus ejecting OH^- and CO_3^{2-} back into solution) and reduction processes produces a locally higher $[OH^-]$, both of which contribute to the increase in pH again. The presence of malachite may not only affect the

https://dx.doi.org/10.1021/acscatal.0c04297
ACS Catal. 2021, 11, 255−263

speciation of CO_2RR products by changing surface sites on the catalyst but also by subtly changing the local pH environment. We note that although this Cu dissolution behavior is the case for the electrodeposited Cu used in this work, the copper oxide speciation has been shown to vary widely depending on the morphology.[58] This work highlights the importance of Cu preparation and the relative speciation of oxides prior to use in CO_2RR in controlling the local pH and surface site availability.

5. CONCLUSIONS

In this work, we sought to measure the local pH of an electrodeposited Cu GDE undergoing CO_2 reduction under alkaline conditions in a gas diffusion electrolyzer. Under flow conditions, using the as-prepared oxidized Cu electrode, the local pH decreases as a function of applied potential. We were able to correlate the lower pH, associated with the formation of HCO_3^-, with the appearance of malachite. The formation of malachite on the surface of the Cu electrode is due to the dissolution of Cu(II) ions during the initial reduction of CuO. The concomitant consumption of CO_3^{2-} leads to a differential pH of almost 5 pH units from the bulk. Reduction of the malachite layer and/or surface oxides results in a return of the local pH to values >11, owing to the presence of CO_3^{2-}. The malachite layer is quite persistent, even at CO_2RR potentials, and may play a role in speciation of CO_2RR products on CuO-rich surfaces. Additionally, it has been reported that malachite formed from Cu foil had a higher Faradaic efficiency for C_2H_4 than the original Cu foil.[59]

This work highlights the fact that, while certain oxidized phases on Cu under CO_2 reducing conditions are not thermodynamically expected via the Cu−CO_2−H_2O Pourbaix diagram, they still could be present, presumably because of their sluggish reduction kinetics.[16] Initially, this work set out to determine the alkaline flow electrolyzer's ability to maintain a basic pH under CO_2 reduction conditions. Although alkaline conditions would not be possible in a H-cell under CO_2 reduction conditions because of solution equilibrium reactions (eqs 1−4), this work demonstrates that the alkaline flow electrolyzer can maintain a local pH that is at least as basic as CO_3^{2-}, even at high current densities more negative than −20 mA/cm^2. Future work will focus on investigating the local pH of different Cu phases and morphologies and associated CO_2RR product selectivity. These results also highlight the very different properties electrocatalytic interfaces can have over local composition of the electrolyte.

■ ASSOCIATED CONTENT

Supporting Information

The Supporting Information is available free of charge at https://pubs.acs.org/doi/10.1021/acscatal.0c04297.

SERS peak integration at different potentials, SERS spectra over time at −1.2 V, SEM before and after electrolysis, data from k_a and k_d fitting, SERS after malachite reduction under CO_2 reducing conditions, and kinetic modeling details (PDF)

■ AUTHOR INFORMATION

Corresponding Authors

Paul J. A. Kenis − *Department of Chemical & Biomolecular Engineering, University of Illinois at Urbana-Champaign, Urbana 61801, Illinois, United States; International Institute for Carbon Neutral Energy Research (WPI-I2CNER), Kyushu University, Fukuoka, Japan;* orcid.org/0000-0001-7348-0381; Email: kenis@illinois.edu

Andrew A. Gewirth − *Department of Chemistry, University of Illinois at Urbana-Champaign, Urbana 61801, Illinois, United States; International Institute for Carbon Neutral Energy Research (WPI-I2CNER), Kyushu University, Fukuoka, Japan;* orcid.org/0000-0003-4400-9907; Email: agewirth@illinois.edu

Authors

Danielle A. Henckel − *Department of Chemistry, University of Illinois at Urbana-Champaign, Urbana 61801, Illinois, United States; Department of Chemical & Biomolecular Engineering, University of Illinois at Urbana-Champaign, Urbana 61801, Illinois, United States*

Michael J. Counihan − *Department of Chemistry, University of Illinois at Urbana-Champaign, Urbana 61801, Illinois, United States*

Hannah E. Holmes − *Department of Chemical & Biomolecular Engineering, University of Illinois at Urbana-Champaign, Urbana 61801, Illinois, United States*

Xinyi Chen − *Department of Chemistry, University of Illinois at Urbana-Champaign, Urbana 61801, Illinois, United States; International Institute for Carbon Neutral Energy Research (WPI-I2CNER), Kyushu University, Fukuoka, Japan;* orcid.org/0000-0002-6990-5233

Uzoma O. Nwabara − *Department of Chemical & Biomolecular Engineering, University of Illinois at Urbana-Champaign, Urbana 61801, Illinois, United States; International Institute for Carbon Neutral Energy Research (WPI-I2CNER), Kyushu University, Fukuoka, Japan*

Sumit Verma − *Shell International Exploration and Production Inc., Houston 77082, Texas, United States*

Joaquín Rodríguez-López − *Department of Chemistry, University of Illinois at Urbana-Champaign, Urbana 61801, Illinois, United States;* orcid.org/0000-0003-4346-4668

Complete contact information is available at: https://pubs.acs.org/10.1021/acscatal.0c04297

Notes

The authors declare no competing financial interest.

■ ACKNOWLEDGMENTS

The authors gratefully acknowledge Shell's New Energies Research and Technology (NERT) Dense Energy Carriers program for providing funding, as well as the support of the International Institute for Carbon Neutral Energy Research (WPI-I2CNER), sponsored by the Japanese Ministry of Education, Culture, Sports, Science and Technology. The authors also thank the School of Chemical Sciences machine shop for their help in designing the in-situ flow cell for the SERS measurements.

■ REFERENCES

(1) Verma, S.; Kim, B.; Jhong, H.-R. M.; Ma, S.; Kenis, P. J. A. A Gross-Margin Model for Defining Technoeconomic Benchmarks in the Electroreduction of CO_2. *ChemSusChem* **2016**, *9*, 1972−1979.

(2) Verma, S.; Lu, S.; Kenis, P. J. A. Co-Electrolysis of CO_2 and Glycerol as a Pathway to Carbon Chemicals with Improved Technoeconomics Due to Low Electricity Consumption. *Nat. Energy* **2019**, *4*, 466.

(3) De Luna, P.; Hahn, C.; Higgins, D.; Jaffer, S. A.; Jaramillo, T. F.; Sargent, E. H. What Would It Take for Renewably Powered

Electrosynthesis to Displace Petrochemical Processes? *Science* **2019**, *364*, No. eaav3506.
(4) Nitopi, S.; Bertheussen, E.; Scott, S. B.; Liu, X.; Engstfeld, A. K.; Horch, S.; Seger, B.; Stephens, I. E. L.; Chan, K.; Hahn, C.; Nørskov, J. K.; Jaramillo, T. F.; Chorkendorff, I. Progress and Perspectives of Electrochemical CO_2 Reduction on Copper in Aqueous Electrolyte. *Chem. Rev.* **2019**, *119*, 7610−7672.
(5) Higgins, D.; Hahn, C.; Xiang, C.; Jaramillo, T. F.; Weber, A. Z. Gas-Diffusion Electrodes for Carbon Dioxide Reduction: A New Paradigm. *ACS Energy Lett.* **2019**, *4*, 317−324.
(6) Dinh, C.-T.; Burdyny, T.; Kibria, M. G.; Seifitokaldani, A.; Gabardo, C. M.; García de Arquer, F. P.; Kiani, A.; Edwards, J. P.; De Luna, P.; Bushuyev, O. S.; Zou, C.; Quintero-Bermudez, R.; Pang, Y.; Sinton, D.; Sargent, E. H. CO_2 Electroreduction to Ethylene via Hydroxide-Mediated Copper Catalysis at an Abrupt Interface. *Science* **2018**, *360*, 783−787.
(7) Bhargava, S. S.; Proietto, F.; Azmoodeh, D.; Cofell, E. R.; Henckel, D. A.; Verma, S.; Brooks, C. J.; Gewirth, A. A.; Kenis, P. J. A. System Design Rules for Intensifying the Electrochemical Reduction of CO2 to CO on Ag Nanoparticles. *ChemElectroChem* **2020**, *7*, 2001−2011.
(8) Kas, R.; Kortlever, R.; Yılmaz, H.; Koper, M. T. M.; Mul, G. Manipulating the Hydrocarbon Selectivity of Copper Nanoparticles in CO_2 Electroreduction by Process Conditions. *ChemElectroChem* **2015**, *2*, 354−358.
(9) Singh, M. R.; Kwon, Y.; Lum, Y.; Ager, J. W.; Bell, A. T. Hydrolysis of Electrolyte Cations Enhances the Electrochemical Reduction of CO_2 over Ag and Cu. *J. Am. Chem. Soc.* **2016**, *138*, 13006−13012.
(10) Varela, A. S.; Kroschel, M.; Reier, T.; Strasser, P. Controlling the Selectivity of CO_2 Electroreduction on Copper: The Effect of the Electrolyte Concentration and the Importance of the Local pH. *Catal. Today* **2016**, *260*, 8−13.
(11) Hori, Y.; Murata, A.; Takahashi, R. Formation of Hydrocarbons in the Electrochemical Reduction of Carbon Dioxide at a Copper Electrode in Aqueous Solution. *J. Chem. Soc., Faraday Trans. 1* **1989**, *85*, 2309−2326.
(12) Murata, A.; Hori, Y. Product Selectivity Affected by Cationic Species in Electrochemical Reduction of CO_2 and CO at a Cu Electrode. *Bull. Chem. Soc. Jpn.* **1991**, *64*, 123−127.
(13) Liu, X.; Schlexer, P.; Xiao, J.; Ji, Y.; Wang, L.; Sandberg, R. B.; Tang, M.; Brown, K. S.; Peng, H.; Ringe, S.; Hahn, C.; Jaramillo, T. F.; Nørskov, J. K.; Chan, K. pH Effects on the Electrochemical Reduction of $CO(_2)$ towards C_2 Products on Stepped Copper. *Nat. Commun.* **2019**, *10*, 32.
(14) Weng, L.-C.; Bell, A. T.; Weber, A. Z. Modeling Gas-Diffusion Electrodes for CO_2 Reduction. *Phys. Chem. Chem. Phys.* **2018**, *20*, 16973−16984.
(15) Lu, X.; Zhu, C.; Wu, Z.; Xuan, J.; Francisco, J. S.; Wang, H. In-Situ Observation of the pH Gradient near the Gas Diffusion Electrode of CO_2 Reduction in Alkaline Electrolyte. *J. Am. Chem. Soc.* **2020**, *142*, 15438−15444.
(16) Mistry, H.; Varela, A. S.; Bonifacio, C. S.; Zegkinoglou, I.; Sinev, I.; Choi, Y.-W.; Kisslinger, K.; Stach, E. A.; Yang, J. C.; Strasser, P.; Cuenya, B. R. Highly Selective Plasma-Activated Copper Catalysts for Carbon Dioxide Reduction to Ethylene. *Nat. Commun.* **2016**, *7*, 12123.
(17) Van Muylder, J. Thermodynamics of Corrosion. *Electrochemical Materials Science*; Springer, 1981; pp 1−96.
(18) Yang, K.; Kas, R.; Smith, W. A. In Situ Infrared Spectroscopy Reveals Persistent Alkalinity near Electrode Surfaces during CO_2 Electroreduction. *J. Am. Chem. Soc.* **2019**, *141*, 15891−15900.
(19) Dunwell, M.; Yang, X.; Setzler, B. P.; Anibal, J.; Yan, Y.; Xu, B. Examination of Near-Electrode Concentration Gradients and Kinetic Impacts on the Electrochemical Reduction of CO_2 Using Surface-Enhanced Infrared Spectroscopy. *ACS Catal.* **2018**, *8*, 3999−4008.
(20) Zhang, F.; Co, A. C. Direct Evidence of Local pH Change and the Role of Alkali Cation during CO_2 Electroreduction in Aqueous Media. *Angew. Chem., Int. Ed.* **2020**, *59*, 1674−1681.
(21) Zhang, Z.; Melo, L.; Jansonius, R. P.; Habibzadeh, F.; Grant, E. R.; Berlinguette, C. P. pH Matters When Reducing CO_2 in an Electrochemical Flow Cell. *ACS Energy Lett.* **2020**, *5*, 3101−3107.
(22) Willets, K. A.; Van Duyne, R. P. Localized Surface Plasmon Resonance Spectroscopy and Sensing. *Annu. Rev. Phys. Chem.* **2007**, *58*, 267−297.
(23) Hoang, T. T. H.; Ma, S.; Gold, J. I.; Kenis, P. J. A.; Gewirth, A. A. Nanoporous Copper Films by Additive-Controlled Electrodeposition: CO_2 Reduction Catalysis. *ACS Catal.* **2017**, *7*, 3313−3321.
(24) Jhong, H.-R. M.; Brushett, F. R.; Kenis, P. J. A. The Effects of Catalyst Layer Deposition Methodology on Electrode Performance. *Adv. Energy Mater.* **2013**, *3*, 589−599.
(25) Chen, X.; Henckel, D. A.; Nwabara, U. O.; Li, Y.; Frenkel, A. I.; Fister, T. T.; Kenis, P. J. A.; Gewirth, A. A. Controlling Speciation during CO_2 Reduction on Cu-Alloy Electrodes. *ACS Catal.* **2020**, *10*, 672−682.
(26) Rooney, R. T.; Jha, H.; Rohde, D.; Schmidt, R.; Gewirth, A. A. Suppression of Copper Electrodeposition by PEG in Methanesulfonic Acid Electrolytes. *J. Electrochem. Soc.* **2019**, *166*, D551−D558.
(27) Rooney, R. T.; Schmitt, K. G.; von Horsten, H. F.; Schmidt, R.; Gewirth, A. A. Raman and QCM Studies of PPG and PEG Adsorption on Cu Electrode Surfaces. *J. Electrochem. Soc.* **2018**, *165*, D687−D695.
(28) Davis, A. R.; Oliver, B. G. A Vibrational-Spectroscopic Study of the Species Present in the CO_2−H_2O System. *J. Solution Chem.* **1972**, *1*, 329−339.
(29) Frantz, J. D. Raman Spectra of Potassium Carbonate and Bicarbonate Aqueous Fluids at Elevated Temperatures and Pressures: Comparison with Theoretical Simulations. *Chem. Geol.* **1998**, *152*, 211−225.
(30) Chernyshova, I. V.; Somasundaran, P.; Ponnurangam, S. On the Origin of the Elusive First Intermediate of CO_2 Electroreduction. *Proc. Natl. Acad. Sci. U.S.A.* **2018**, *115*, E9261−E9270.
(31) Wang, L.; Gupta, K.; Goodall, J. B. M.; Darr, J. A.; Holt, K. B. In Situ Spectroscopic Monitoring of CO_2 Reduction at Copper Oxide Electrode. *Faraday Discuss.* **2017**, *197*, 517−532.
(32) Jiang, S.; Klingan, K.; Pasquini, C.; Dau, H. New Aspects of Operando Raman Spectroscopy Applied to Electrochemical CO_2 Reduction on Cu Foams. *J. Chem. Phys.* **2019**, *150*, 041718.
(33) Frost, R. L.; Martens, W. N.; Rintoul, L.; Mahmutagic, E.; Kloprogge, J. T. Raman Spectroscopic Study of Azurite and Malachite at 298 and 77 K. *J. Raman Spectrosc.* **2002**, *33*, 252−259.
(34) Becerra, J. G.; Salvarezza, R. C.; Arvia, A. J. The Influence of Slow $Cu(OH)_2$ Phase Formation on the Electrochemical Behaviour of Copper in Alkaline Solutions. *Electrochim. Acta* **1988**, *33*, 613−621.
(35) Maurice, V.; Strehblow, H.-H.; Marcus, P. In Situ STM Study of the Initial Stages of Oxidation of Cu (111) in Aqueous Solution. *Surf. Sci.* **2000**, *458*, 185−194.
(36) Deng, Y.; Handoko, A. D.; Du, Y.; Xi, S.; Yeo, B. S. In Situ Raman Spectroscopy of Copper and Copper Oxide Surfaces during Electrochemical Oxygen Evolution Reaction: Identification of CuIII Oxides as Catalytically Active Species. *ACS Catal.* **2016**, *6*, 2473−2481.
(37) Singhal, A.; Pai, M. R.; Rao, R.; Pillai, K. T.; Lieberwirth, I.; Tyagi, A. K. Copper(I) Oxide Nanocrystals − One Step Synthesis, Characterization, Formation Mechanism, and Photocatalytic Properties. *Eur. J. Inorg. Chem.* **2013**, *2013*, 2640−2651.
(38) Chan, H. Y. H.; Takoudis, C. G.; Weaver, M. J. Oxide Film Formation and Oxygen Adsorption on Copper in Aqueous Media as Probed by Surface-Enhanced Raman Spectroscopy. *J. Phys. Chem. B* **1999**, *103*, 357−365.
(39) Debbichi, L.; Marco de Lucas, M. C.; Pierson, J. F.; Krüger, P. Vibrational Properties of CuO and Cu_4O_3 from First-Principles Calculations, and Raman and Infrared Spectroscopy. *J. Phys. Chem. C* **2012**, *116*, 10232−10237.
(40) Adeloju, S. B.; Hughes, H. C. The Corrosion of Copper Pipes in High Chloride-Low Carbonate Mains Water. *Corros. Sci.* **1986**, *26*, 851−870.

https://dx.doi.org/10.1021/acscatal.0c04297
ACS Catal. 2021, 11, 255−263

(41) Strehblow, H.-H.; Maurice, V.; Marcus, P. Initial and Later Stages of Anodic Oxide Formation on Cu, Chemical Aspects, Structure and Electronic Properties. *Electrochim. Acta* **2001**, *46*, 3755−3766.
(42) Kunze, J.; Maurice, V.; Klein, L. H.; Strehblow, H.-H.; Marcus, P. In Situ Scanning Tunneling Microscopy Study of the Anodic Oxidation of Cu (111) in 0.1 M NaOH. *J. Phys. Chem. B* **2001**, *105*, 4263−4269.
(43) Kang, M.; Gewirth, A. A. Voltammetric and Force Spectroscopic Examination of Oxide Formation on Cu (111) in Basic Solution. *J. Phys. Chem. B* **2002**, *106*, 12211−12220.
(44) De Chialvo, M. R. G.; Marchiano, S. L.; Arvía, A. J. The Mechanism of Oxidation of Copper in Alkaline Solutions. *J. Appl. Electrochem.* **1984**, *14*, 165−175.
(45) Shoesmith, D. W.; Rummery, T. E.; Owen, D.; Lee, W. Anodic Oxidation of Copper in Alkaline Solutions: I. Nucleation and Growth of Cupric Hydroxide Films. *J. Electrochem. Soc.* **1976**, *123*, 790.
(46) Brisard, G. M.; Rudnicki, J. D.; Mclarnon, F.; Cairns, E. J. Application of Probe Beam Deflection to Study the Electrooxidation of Copper in Alkaline Media. *Electrochim. Acta* **1995**, *40*, 859−865.
(47) Burke, L. D.; Ahern, M. J. G.; Ryan, T. G. An Investigation of the Anodic Behavior of Copper and Its Anodically Produced Oxides in Aqueous Solutions of High pH. *J. Electrochem. Soc.* **1990**, *137*, 553.
(48) Sun, J.-M.; Zhao, X.-H.; Huang, J.-C. Characterization of Adsorbent Composition in Co-Removal of Hexavalent Chromium with Copper Precipitation. *Chemosphere* **2005**, *58*, 1003−1010.
(49) Patterson, J. W. Effect of Carbonate Ion on Precipitation Treatment of Cadmium, Copper, Lead and Zinc. *Proceedings of the Industrial Waste Conference;(United States)*; Illinois Institute of Technology: Chicago, 1982; Vol. *36*.
(50) Symes, J. L.; Kester, D. R. Copper (II) Interaction with Carbonate Species Based on Malachite Solubility in Perchlorate Medium at the Ionic Strength of Seawater. *Mar. Chem.* **1985**, *16*, 189−211.
(51) Powell, K. J.; Brown, P. L.; Byrne, R. H.; Gajda, T.; Hefter, G.; Sjöberg, S.; Wanner, H. Chemical Speciation of Environmentally Significant Metals with Inorganic Ligands Part 2: The Cu^{2+}-OH^-, Cl^-, CO_3^{2-}, SO_4^{2-}, and PO_4^{3-} Systems (IUPAC Technical Report). *Pure Appl. Chem.* **2007**, *79*, 895−950.
(52) Malvault, J. Y.; Lopitaux, J.; Delahaye, D.; Lenglet, M. Cathodic Reduction and Infrared Reflectance Spectroscopy of Basic Copper (II) Salts on Copper Substrate. *J. Appl. Electrochem.* **1995**, *25*, 841−845.
(53) Schulz, K. G.; Riebesell, U.; Rost, B.; Thoms, S.; Zeebe, R. E. Determination of the Rate Constants for the Carbon Dioxide to Bicarbonate Inter-Conversion in pH-Buffered Seawater Systems. *Mar. Chem.* **2006**, *100*, 53−65.
(54) Young, A. G.; McQuillan, A. J. Adsorption/Desorption Kinetics from ATR-IR Spectroscopy. Aqueous Oxalic Acid on Anatase TiO_2. *Langmuir* **2009**, *25*, 3538−3548.
(55) Bockris, J. M.; Conway, B. E. *Electrochemical Materials Science (Comprehensive Treatise of Electrochemistry)*; Plenum Press: New York and London, Vol. *4*, 1981.
(56) Lenormand, J.; Salman, T.; Yoon, R. H. Hydroxamate Flotation of Malachite. *Can. Metall. Q.* **1979**, *18*, 125−129.
(57) Łukomska, A.; Sobkowski, J. Potential of Zero Charge of Monocrystalline Copper Electrodes in Perchlorate Solutions. *J. Electroanal. Chem.* **2004**, *567*, 95−102.
(58) Zhao, Y.; Chang, X.; Malkani, A.; Yang, X.; Thompson, L.; Jiao, F.; Xu, B. Speciation of Cu Surfaces During the Electrochemical CO Reduction Reaction. *J. Am. Chem. Soc.* **2020**, *142*, 9735−9743.
(59) Spodaryk, M.; Zhao, K.; Zhang, J.; Oveisi, E.; Züttel, A. The Role of Malachite Nanorods for the Electrochemical Reduction of CO_2 to C_2 Hydrocarbons. *Electrochim. Acta* **2019**, *297*, 55−60.

https://dx.doi.org/10.1021/acscatal.0c04297
ACS Catal. 2021, 11, 255−263